



Volatile-rich Sub-Neptunes as Hydrothermal Worlds: The Case of K2-18 b

Cindy N. Luu¹ , Xinting Yu (余馨婷)¹ , Christopher R. Glein² , Hamish Innes^{3,4} , Artyom Aguchine⁵ , Joshua Krissansen-Totton⁶ , Julianne I. Moses⁷ , Shang-Min Tsai⁸ , Xi Zhang⁹ , Ngoc Truong² , and Jonathan J. Fortney⁵

¹ Department of Physics and Astronomy, University of Texas at San Antonio, 1 UTSA Circle, San Antonio, TX 78249, USA; xinting.yu@utsa.edu

² Space Science Division, Southwest Research Institute, 6220 Culebra Rd., San Antonio, TX 78238, USA

³ Institute for Geological Sciences, Freie Universität Berlin, Malteserstr. 74-100, 12249 Berlin, Germany

⁴ Department of Extrasolar Planets and Atmospheres, German Aerospace Centre (DLR), Rutherfordstraße 2, 12489 Berlin, Germany

⁵ Department of Astronomy and Astrophysics, University of California Santa Cruz, 1156 High St., Santa Cruz, CA 95064, USA

⁶ Department of Earth and Space Sciences, University of Washington, Seattle, 1410 NE Campus Pkwy., Seattle, WA 98195, USA

⁷ Space Science Institute, Boulder, CO 80301, USA

⁸ Department of Earth and Planetary Sciences, University of California Riverside, 900 University Ave., Riverside, CA 92521, USA

⁹ Department of Earth and Planetary Sciences, University of California Santa Cruz, 1156 High St., Santa Cruz, CA 95064, USA

Received 2024 September 10; revised 2024 December 03; accepted 2024 December 08; published 2024 December 27

Abstract

Temperate exoplanets between the sizes of Earth and Neptune, known as “sub-Neptunes,” have emerged as intriguing targets for astrobiology. It is unknown whether these planets resemble Earth-like terrestrial worlds with a habitable surface, Neptune-like giant planets with deep atmospheres and no habitable surface, or something exotic in between. Recent JWST transmission spectroscopy observations of the canonical sub-Neptune, K2-18 b, revealed ~1% CH₄, ~1% CO₂, and a nondetection of CO in the atmosphere. While previous studies proposed that the observed atmospheric composition could help constrain the lower atmosphere’s conditions and determine the interior structure of sub-Neptunes like K2-18 b, the possible interactions between the atmosphere and a hot, supercritical water ocean at its base remain unexplored. In this work, we investigate whether a global supercritical water ocean, resembling a planetary-scale hydrothermal system, can explain these observations on K2-18 b—like sub-Neptunes through equilibrium aqueous geochemical calculations. We find that the observed atmospheric CH₄/CO₂ ratio implies a minimum ocean temperature of ~710 K, whereas the corresponding CO/CO₂ ratio allows ocean temperatures up to ~1070 K. These results indicate that a global supercritical water ocean on K2-18 b is plausible. While life cannot survive in such an ocean, this work represents the first step toward understanding how a global supercritical water ocean may influence observable atmospheric characteristics on volatile-rich sub-Neptunes. Future observations with better-constrained CO and NH₃ mixing ratios could further help distinguish between possible interior compositions of K2-18 b.

Unified Astronomy Thesaurus concepts: [Exoplanets \(498\)](#); [Exoplanet atmospheres \(487\)](#); [Exoplanet atmospheric structure \(2310\)](#); [Planetary atmospheres \(1244\)](#); [Astrobiology \(74\)](#); [Ocean planets \(1151\)](#); [James Webb Space Telescope \(2291\)](#); [Exoplanet surfaces \(2118\)](#); [Extrasolar gaseous planets \(2172\)](#)

1. Introduction

Understanding the compositions of exoplanets is crucial for identifying potentially habitable worlds. The majority of confirmed exoplanets are classified as sub-Neptunes—exoplanets between the sizes of Earth and Neptune—that are unlike any planetary body in our solar system (F. Fressin et al. 2013; N. M. Batalha 2014; J. N. Winn & D. C. Fabrycky 2015; B. J. Fulton et al. 2017). Because a range of interior compositions can explain the observed masses and radii of sub-Neptunes, it is unknown whether these planets are closer to (1) terrestrial planets with thin atmospheres and potentially habitable surfaces; (2) “mini-Neptunes,” which are less massive versions of our solar system’s ice giants; or (3) “in-between state” planets, such as “water worlds” with volatile-rich interiors. Among the sub-Neptune population, the canonical habitable-zone sub-Neptune K2-18 b has captured the attention of the astrobiology community (C. R. Glein 2024).

K2-18 b has a radius of $2.610 \pm 0.087 R_{\oplus}$ (B. Benneke et al. 2019), a mass of $8.63 \pm 1.35 M_{\oplus}$ (R. Cloutier et al. 2019), and a bulk density of $2.67^{+0.52}_{-0.47} \text{ g cm}^{-3}$ (B. Benneke et al. 2019) that can be explained by a diverse range of interior structures with varying amounts of H₂O and H₂/He in a volatile-rich envelope (N. Madhusudhan et al. 2020; M. C. Nixon & N. Madhusudhan 2021; F. E. Rigby et al. 2024). To discern the most plausible structure, previous studies proposed that the observed atmospheric composition could be key to understanding the conditions at the base of the atmosphere in temperate sub-Neptunes (R. Hu et al. 2021; S.-M. Tsai et al. 2021; X. Yu et al. 2021; N. Madhusudhan et al. 2023a). Potential atmospheric compositions have been explored for various possible atmosphere–interior structure scenarios (as shown in Figure 1), including a thin-atmosphere rocky world (S.-M. Tsai et al. 2021; X. Yu et al. 2021), a thin-atmosphere liquid water world with potential signs of life (known as a “Hycean” world; R. Hu et al. 2021; N. Madhusudhan et al. 2023b; G. J. Cooke & N. Madhusudhan 2024; S.-M. Tsai et al. 2024; N. F. Wogan et al. 2024), a deep-atmosphere mini-Neptune with no surface (R. Hu 2021; S.-M. Tsai et al. 2021; X. Yu et al. 2021; N. F. Wogan et al. 2024), and a deep-atmosphere mini-Neptune with a silicate magma ocean (O. Shorttle et al. 2024). While the

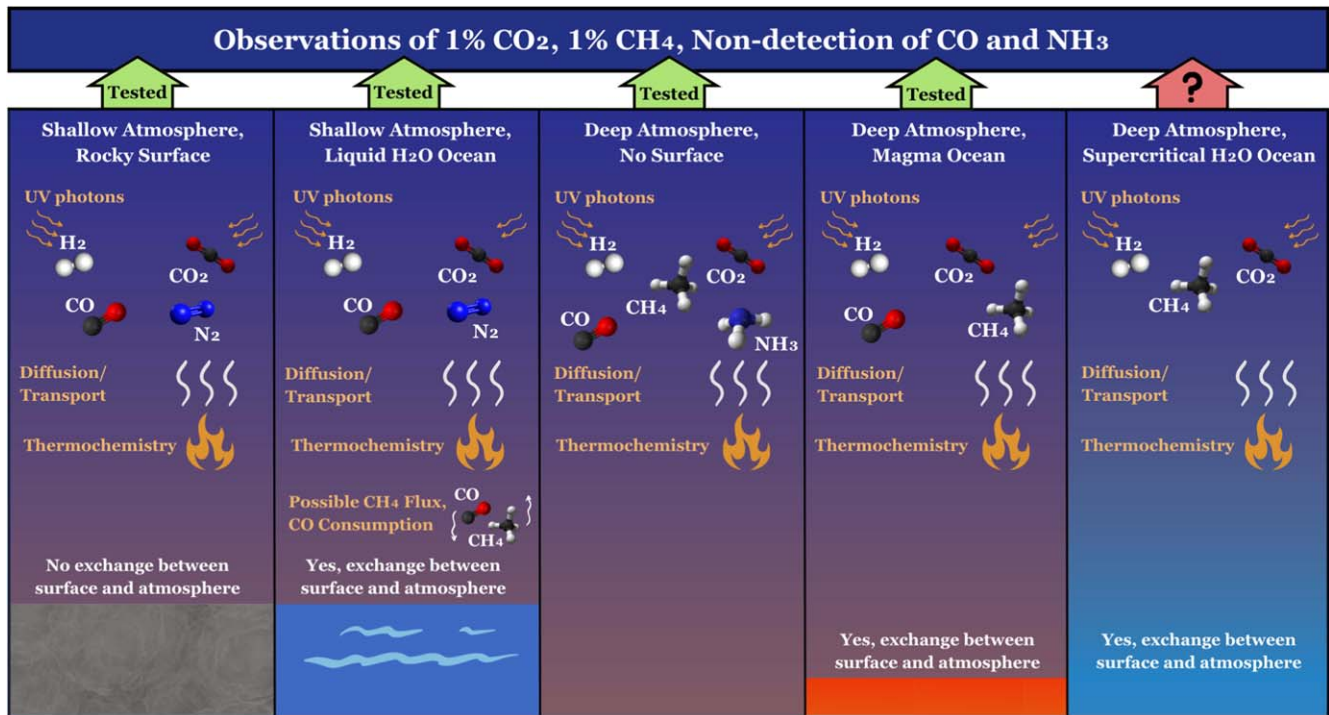


Figure 1. Possible conceptual structures for K2-18 b that were explored previously (R. Hu 2021; R. Hu et al. 2021; S.-M. Tsai et al. 2021; X. Yu et al. 2021; N. Madhusudhan et al. 2023b; G. J. Cooke & N. Madhusudhan 2024; F. E. Rigby et al. 2024; O. Shorttle et al. 2024; N. F. Wogan et al. 2024) and in this work.

rocky world scenario was found to be inconsistent with observations (N. Madhusudhan et al. 2020), the water world and mini-Neptune scenarios remain possible.

Recent JWST transmission spectroscopy of K2-18 b led to the first detection of CH_4 (~1%) and CO_2 (~1%) in the atmosphere of a sub-Neptune, along with nondetections of H_2O , CO , and NH_3 (N. Madhusudhan et al. 2023b). Despite all of the excellent work that has been done, existing models have struggled to fully explain this observed atmospheric composition. Recent predictions suggest that K2-18 b's interior may be water-rich (J. Yang & R. Hu 2024), and sub-Neptunes with close orbits could host supercritical water oceans (O. Mousis et al. 2020). Climate models also predict that “Hycean worlds” ($T_{\text{eq}} < 500$ K; N. Madhusudhan et al. 2021) receiving solar-like flux with pure H_2 -He atmospheres will experience runaway greenhouse effects, driving surface water to a supercritical state (H. Innes et al. 2023; R. T. Pierrehumbert 2023; J. Lecante et al. 2024). However, the atmospheric interactions with a global supercritical water ocean remain largely unexplored. Pure water reaches its critical point at 220.64 bars and 647.096 K (W. Wagner & A. Pruß 2002), beyond which there is no distinction between liquid and gas. On K2-18 b, an ocean of supercritical water would manifest as a layer of hot aqueous fluids merging seamlessly with the H_2 -dominated atmosphere above, potentially creating a global hydrothermal environment. In this regime, we consider two distinct structures containing supercritical water to be likely. At lower pressures, H_2 is miscible with water (T. M. Seward & E. U. Franck 1981; H. Innes et al. 2023; R. T. Pierrehumbert 2023; A. Gupta et al. 2024) and creates a homogeneous supercritical H_2 - H_2O ocean. At higher pressures, H_2 and H_2O may be immiscible and could separate into a distinct supercritical H_2O -rich layer beneath a supercritical H_2 -rich layer (A. Gupta et al. 2024). Current photochemical models do not account for interactions between an H_2 atmosphere and a supercritical water or hydrogen layer

(R. Hu 2021; S.-M. Tsai et al. 2021; X. Yu et al. 2021; N. Madhusudhan et al. 2023a, 2023b), highlighting the need for new approaches. Our study addresses this gap by exploring the geochemistry in a supercritical water ocean on K2-18 b in an attempt to explain the observed abundances of key species in K2-18 b's atmosphere. We focus on major carbon species, as their abundances are well constrained by existing observations (N. Madhusudhan et al. 2023b).

2. Methodology

We aim to derive constraints on the boundary conditions at the transition region between the atmosphere and a hypothetical supercritical water ocean. To explore how ocean conditions could drive volatile chemistry, we first calculate the aqueous equilibrium ratios of CH_4/CO_2 and CO/CO_2 in the supercritical water ocean, as detailed in Section 2.1. Given the likely absence of a distinct boundary between the supercritical water ocean and the gaseous atmosphere, we conduct the aqueous calculations at temperatures and pressures where chemical equilibrium could be achieved. Consequently, the term “ocean temperature” in this study refers to the condition for reaching an apparent chemical equilibrium rather than a discrete physical boundary between the ocean and the atmosphere.

Building on the aqueous results, we then explore how the aqueous ratios translate to the observable atmosphere. To achieve this, we performed exsolution calculations to predict the gaseous ratios of carbon-bearing species in the atmosphere, as detailed in Section 2.3 (see also Figure 2(b)). By comparing the predicted gaseous ratios to the observed species abundances in the atmosphere, we can determine whether a set of conditions in the supercritical water ocean would satisfy observational constraints.

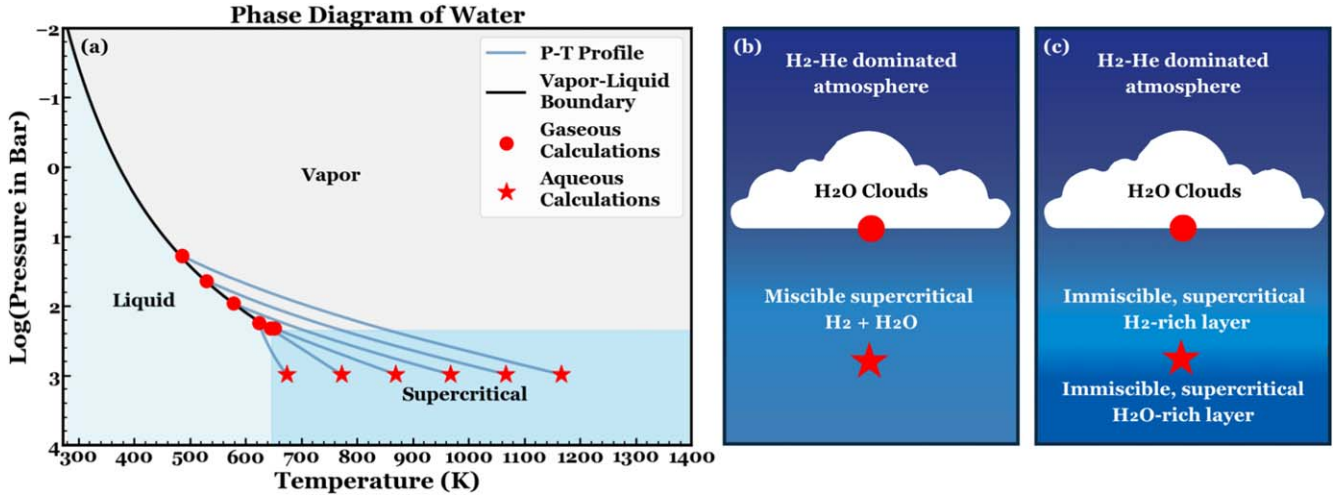
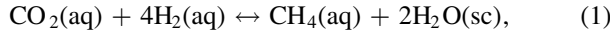


Figure 2. (a) Phase diagram of pure water, showing adiabats for six selected ocean temperatures from 647.15 K to 1273.15 K at a pressure of redox equilibrium of 1 kbar as an example. This plot is most relevant to cases with lower H_2 abundances in the fluid envelope. Liquid water will be saturated at lower temperatures for the highest H_2 abundance considered in this work (see Appendix G). (b) A schematic diagram showing the upper interior structure of K2-18 b with a miscible supercritical $\text{H}_2 + \text{H}_2\text{O}$ layer (B. Benneke et al. 2024) or (c) with phase-separated H_2 -rich and H_2O -rich layers and a cloud layer in an H_2 -He-dominated atmosphere. Star and circle symbols represent where aqueous and gaseous calculations are performed, respectively.

2.1. Aqueous Chemistry of Carbon

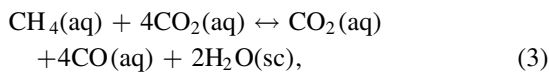
At chemical equilibrium, the molar ratio of CH_4/CO_2 can be computed as a function of temperature, total pressure, and fluid oxidation state. In an H_2 -rich environment such as K2-18 b, the oxidation state can be effectively represented by the molal concentration of hydrogen gas dissolved in the ocean. The reaction that describes the chemical equilibrium between CO_2 and CH_4 in an H_2 -bearing supercritical fluid can be written as



$$K_1 = \left(\frac{a_{\text{CH}_4}}{a_{\text{CO}_2}} \right) \frac{(a_{\text{H}_2\text{O}})^2}{(a_{\text{H}_2})^4} \approx \left(\frac{m_{\text{CH}_4}}{m_{\text{CO}_2}} \right) \frac{(X_{\text{H}_2\text{O}})^2}{(m_{\text{H}_2})^4}, \quad (2)$$

where “sc” refers to the supercritical fluid phase, K stands for the equilibrium constant, a denotes the activity in an aqueous solution, X represents the mole fraction, and m designates the molality, which describes the number of moles of solute per kilogram of H_2O . In Equation (2), following C. R. Glein et al. (2008), we make the following approximations: (1) the activity of water is considered equivalent to the mole fraction of water in the supercritical phase, (2) the activity of H_2 is approximated by the molality of H_2 , and (3) the activity ratio of CO_2 and CH_4 is equivalent to their molality ratio and thus their mole fraction ratio ($X_{\text{CH}_4}/X_{\text{CO}_2}$). Other approximations for water and the aqueous species that reflect thermodynamic standard-state conventions can be found in Appendix D.

To evaluate for internal consistency, the ratio of CO/CO_2 can be estimated using the observed CH_4/CO_2 ratio constraint from N. Madhusudhan et al. (2023b), based on the following reaction:



$$K_2 = \left(\frac{a_{\text{CO}_2}}{a_{\text{CH}_4}} \right) \left(\frac{a_{\text{CO}}}{a_{\text{CO}_2}} \right)^4 (a_{\text{H}_2\text{O}})^2 \approx \left(\frac{m_{\text{CO}_2}}{m_{\text{CH}_4}} \right) \left(\frac{m_{\text{CO}}}{m_{\text{CO}_2}} \right)^4 (X_{\text{H}_2\text{O}})^2. \quad (4)$$

We chose this reaction because the observed mixing ratios of CH_4 and CO_2 make them the most abundant oxygen- and carbon-bearing molecules, and they are also the most well-constrained, while the uncertainty on CO abundance is high. By including CO_2 as both a product and reactant, we can express Equation (4) in terms of the carbon species ratios. This choice ensures that our CO/CO_2 modeling always aligns with the observed CH_4/CO_2 ratio.

Here we implement the Deep Earth Water (DEW) model, originally developed to study the carbon cycle in Earth’s mantle fluids (E. L. Shock & H. C. Helgeson 1988, 1990; D. A. Sverjensky et al. 2014), to calculate equilibrium constants under conditions potentially relevant to K2-18 b and determine the molal ratios of CH_4/CO_2 and CO/CO_2 across wide ranges of temperatures, pressures, and fluid oxidation states. Below, we consider “ocean temperatures” ranging from 374°C up to 1000°C (647.15–1273.15 K), where we reference 647.15 K as the critical temperature of pure water, and three pressure conditions (1 kbar, 5 kbar, and 10 kbar) to understand how key geochemical variables affect aqueous ratios involving CO_2 , CH_4 , and CO at chemical equilibrium.

2.2. Constraining the Range of Hydrogen Molality

To model the CH_4/CO_2 ratios using Equation (2), we require an estimate of the hydrogen molality (m_{H_2} , expressed in molal units, $\text{mol} \cdot (\text{kg H}_2\text{O})^{-1}$), based on the aqueous standard state on K2-18 b. Previous interior structure modeling by N. Madhusudhan et al. (2020) suggests that the overall m_{H_2} of K2-18 b varies widely depending on the planet’s bulk composition, from near-zero for water-dominated interiors to higher values for H-He-dominated cases. Based on these models, combined with planet formation constraints, we estimate m_{H_2} to plausibly range from 0.14 to 56.55 $\text{mol} \cdot (\text{kg H}_2\text{O})^{-1}$, although higher values cannot be excluded. For further details on how these limits were derived, refer to Appendix C.

However, the modeling results using m_{H_2} equal to and above the upper limit should only be interpreted qualitatively in terms of trends, as higher hydrogen molalities describe increasingly

water-poor solutions. These conditions become less applicable to a water-rich supercritical ocean, which is the scenario that can be evaluated based on the assumptions inherent to our aqueous chemistry framework (see Appendix D). As such, an intermediate hydrogen molality of $m_{\text{H}_2} = 6.16 \text{ mol} \cdot (\text{kg H}_2\text{O})^{-1}$ was also selected to represent a mole fraction of 90.0% H_2O and 10.0% H_2 , excluding He in this case. This value is roughly the upper limit that the DEW model can accommodate while preserving the dilute solution assumptions made in the model.

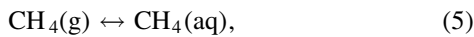
These hydrogen molalities, $m_{\text{H}_2} = 0.14, 6.16,$ and $56.55 \text{ mol} \cdot (\text{kg H}_2\text{O})^{-1}$, correspond to hydrogen mole fractions of $X_{\text{H}_2} = 0.002, 0.100,$ and 0.433 and water mole fractions of $X_{\text{H}_2\text{O}} = 0.996, 0.900,$ and 0.424 , respectively. For the remainder of this paper, we refer to these compositions as $X_{\text{H}_2\text{O}} = 99.6\%, 90.0\%,$ and 42.4% .

2.3. Gaseous Carbon Species from Ocean to Atmosphere

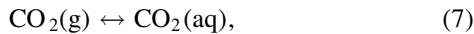
While understanding the carbon ratios in the ocean is an important first step, it is also important to understand how those ratios would be translated to the upper atmosphere, where atmospheric observations are made. K2-18 b presents a special case due to water condensation, which depletes water vapor in the upper atmosphere and creates a distinct cloud layer of liquid water beneath the observable photosphere (B. Benneke et al. 2019; N. Madhusudhan et al. 2023a). Hence, we must apply Henry's law to predict the ratios of atmospheric gases involving CH_4 , CO_2 , and CO .

Henry's law states that the activity of a solute species in a solvent is proportional to the fugacity of the gas in equilibrium with the solution at constant temperature and pressure. In ideal fluids, the fugacity is equivalent to the partial pressure. In this context, water serves as the solvent, and gaseous species (CH_4 , CO_2 , and CO) dissolve in it. Here, we apply Henry's law at the saturation boundary between the liquid and gaseous phases to estimate gas-phase ratios at the base of the cloud layer, where phase partitioning occurs.

The relevant reactions and equations corresponding to Henry's law are shown below:



$$K_{\text{H,CH}_4} \approx \frac{(m_{\text{CH}_4})}{(p_{\text{CH}_4})}, \quad (6)$$



$$K_{\text{H,CO}_2} \approx \frac{(m_{\text{CO}_2})}{(p_{\text{CO}_2})}, \quad (8)$$



$$K_{\text{H,CO}} \approx \frac{(m_{\text{CO}})}{(p_{\text{CO}})}, \quad (10)$$

where K_{H} represents the Henry's law constant and p corresponds to the partial pressure of each species in bars. Using these constants and the aqueous ratios, the gaseous ratio between CH_4/CO_2 and CO/CO_2 can be calculated as

$$\frac{p_{\text{CH}_4}}{p_{\text{CO}_2}} = \left(\frac{K_{\text{H,CO}_2}}{K_{\text{H,CH}_4}} \right) \left(\frac{m_{\text{CH}_4}}{m_{\text{CO}_2}} \right), \quad (11)$$

$$\frac{p_{\text{CO}}}{p_{\text{CO}_2}} = \left(\frac{K_{\text{H,CO}_2}}{K_{\text{H,CO}}} \right) \left(\frac{m_{\text{CO}}}{m_{\text{CO}_2}} \right). \quad (12)$$

To determine the temperature and pressure conditions where gas–liquid partitioning occurs, we began by locating the saturation boundary of water using the Reference Fluid Thermodynamic and Transport Properties (REFPROP) program (M. L. Huber et al. 2022). Then, we generated adiabatic atmospheric pressure–temperature (P-T) profiles to identify where they intersect the saturation boundary. This process is illustrated in Figure 2(a) and detailed further in Appendix E. The intersection between the profiles and the liquid–vapor saturation boundary indicates the approximate location of the cloud deck.

Once the crossing temperature and pressure are determined for each ocean temperature and pressure, we can use the DEW model to evaluate the corresponding Henry's law constant under saturated conditions. The partial pressure ratios are then solved using Equations (11) and (12). Although the gaseous calculations are performed at saturated conditions, they reflect gaseous ratios corresponding to each “ocean temperature” at the bottom boundary, where chemical equilibrium is reached.

3. Results and Discussion

3.1. Can a Supercritical Water Ocean Explain K2-18 b's Atmospheric Chemistry?

Our modeling approach examines both the aqueous and gas phases to evaluate the impact of phase transitions on the ratios of carbon species in K2-18 b's hypothetical supercritical water ocean and in its atmosphere. However, we focus primarily on the results for the gaseous ratios since they correspond most closely to the observed abundances in K2-18 b's upper atmosphere. For the CH_4/CO_2 ratio (Figure 3), our results show that higher ocean temperatures favor the production of CO_2 , while higher pressures and lower water mole fractions (more H_2) promote the formation of CH_4 . We find that the predicted gaseous CH_4/CO_2 ratios indicate a lower temperature limit of $T \approx 710 \text{ K}$ to reproduce the observed CH_4/CO_2 ratio across the full range of H_2 molalities explored. Subcritical temperatures would only be consistent with the measured CH_4/CO_2 ratio if the H_2 abundance were very low, requiring K2-18 b to have an unrealistically high water/rock mass ratio. For the CO/CO_2 ratio (Figure 4), it can be seen that higher temperatures and lower pressures favor the formation of CO . We find that our gaseous CO/CO_2 ratios support temperatures of less than $\sim 1070 \text{ K}$ to avoid exceeding the observational detection limit for CO ($\log(X_{\text{CO}}) < -3.50$ at a 95% upper confidence limit; N. Madhusudhan et al. 2023b).

Combining these constraints then provides a self-consistent ocean temperature range of $T \approx 710\text{--}1070 \text{ K}$, which exceeds the critical temperatures of pure water as well as relevant $\text{H}_2\text{--H}_2\text{O}$ mixtures (T. M. Seward & E. U. Franck 1981). These findings suggest that the presence of a supercritical water ocean can explain the observed carbon ratios in K2-18 b's atmosphere. Between pressures of 1 and 5 kbar, H_2 is completely miscible with water according to A. Gupta et al. (2024), leading to a homogeneous supercritical $\text{H}_2\text{--H}_2\text{O}$ ocean that would categorize K2-18 b as a “Stratified mini-Neptune” as defined by B. Benneke et al. (2024). On the other hand, at pressures between 5 and 10 kbar, H_2 and H_2O may be immiscible at some temperatures, leading to a phase-separated water-rich

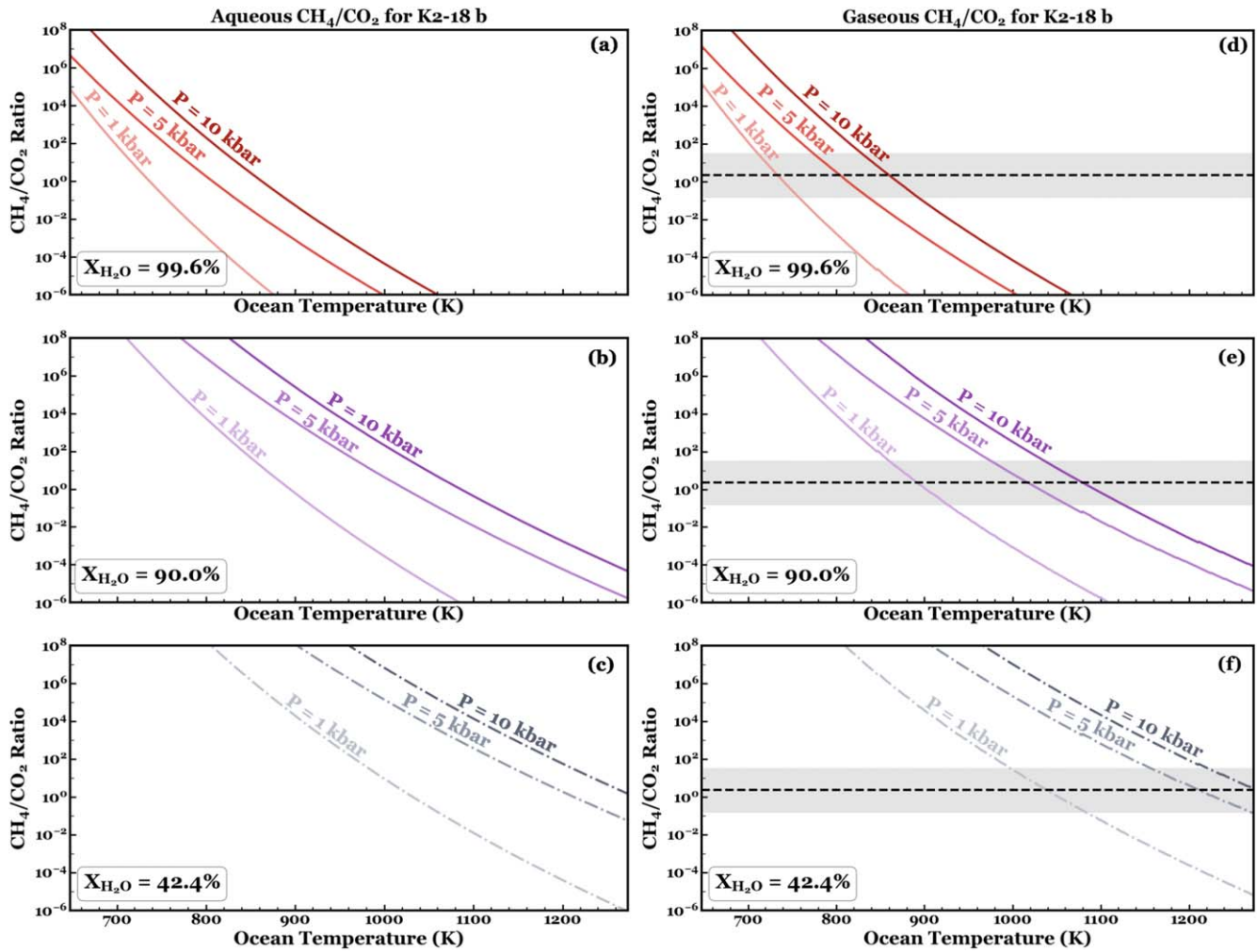


Figure 3. Panels (a)–(c) and panels (d)–(f) show the calculated aqueous and gaseous CH_4/CO_2 ratios at $X_{\text{H}_2\text{O}} = 99.6\%$, 90.0% , and 42.4% . The $X_{\text{H}_2\text{O}} = 42.4\%$ results are in dashed lines to imply that the results are illustrative, as this concentration describes a hydrogen-rich fluid (see Appendix D). The black dashed line and gray region represent the CH_4/CO_2 ratio and uncertainty presented in N. Madhusudhan et al. (2023b).

layer beneath a supercritical H_2 -rich layer (A. Gupta et al. 2024). We discuss more intricate scenarios and their implications further in Appendix G3. This structure would categorize K2-18 b as a mini-Neptune similar to Uranus and Neptune interior models (L. Scheibe et al. 2019; M. Cano Amoros et al. 2024; A. Gupta et al. 2024). Note that unlike “mini-Neptune” gas-phase models that assume deep H_2 -dominated atmospheres for K2-18 b (R. Hu 2021; S.-M. Tsai et al. 2021; X. Yu et al. 2021; J. Leconte et al. 2024; J. Yang & R. Hu 2024), our supercritical ocean chemistry model can explain the low observed abundance of CO on K2-18 b.

Both the lower and upper temperature limits are conservative estimates. Higher pressures than those we explored are possible, and if equilibrium is attained at higher pressures, this may shift the lower limit on temperature upward. In addition, the $\text{CO}-\text{CO}_2$ couple reequilibrates faster than CH_4-CO_2 since the latter reaction requires more bond-breaking and bond-making steps (J. Wei & E. Iglesia 2004); thus, CO may partially reequilibrate in the warm atmosphere above the ocean.

We note that the gaseous results show only subtle differences compared to the aqueous phase for both the CH_4/CO_2 and CO/CO_2 ratios, which aligns with our expectations, given the relatively similar solubilities of CH_4 , CO_2 , and CO in supercritical water. CO_2 is slightly more

soluble in liquid water than CH_4 and CO are, which may cause some fractionation during water cloud condensation. However, this effect diminishes with increasing temperature. As the temperature rises, their respective Henry’s law constants become more similar (see Figure F1). This reduces their differences in solubility and minimizes fractionation. As a result, the ratios in the gaseous phase closely mirror those of the aqueous phase, with only minor variations driven by the slightly higher solubility of CO_2 .

Although our gaseous calculations represent carbon ratios at the cloud interface layer, we can directly compare these results with observed abundances from the region probed by JWST. We assume that the gaseous ratios remain largely unchanged for two main reasons. First, previous photochemical models suggest that these carbon species are quenched at pressures between 10 and 100 bars (R. Hu 2021; S.-M. Tsai et al. 2021; X. Yu et al. 2021; J. Yang & R. Hu 2024), similar to the pressure levels at the base of the cloud layer where our calculations are performed. At pressures lower than the quench point, the mixing ratios of these species remain constant as they are transported upward through the atmosphere until photochemistry becomes important. Since JWST primarily probes the atmosphere at pressures between 0.1 and 2 mbar (Z. Rustamkulov et al. 2023) and multiple photochemical

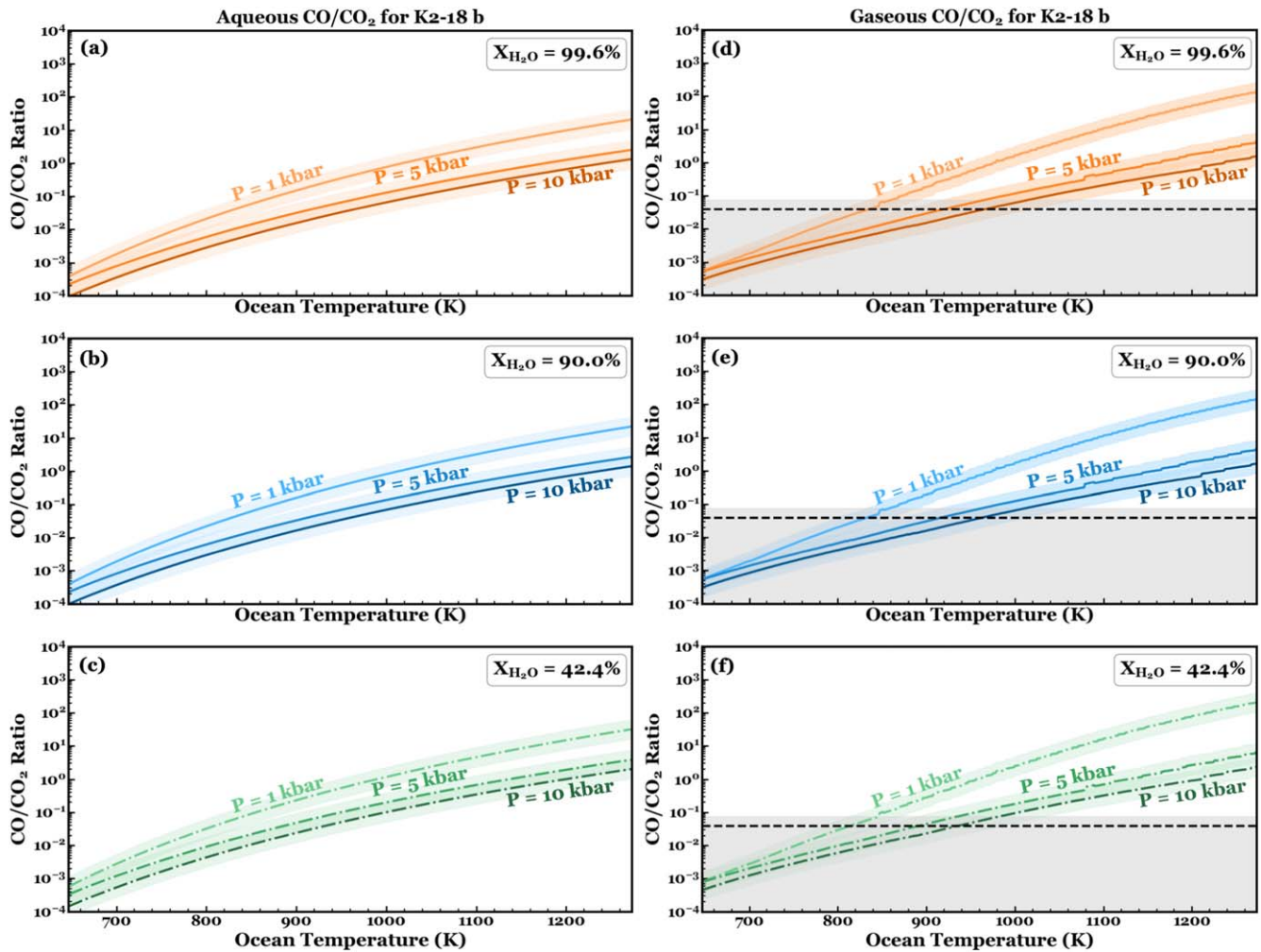


Figure 4. (a)–(c) Aqueous and (d)–(f) gaseous CO/CO₂ ratios. The symbols and colors are labeled the same way as in Figure 3. The region of uncertainty surrounding the curves is due to the one-offset error for the CH₄/CO₂ ratio.

models demonstrate that photochemistry may have minimal influence on the atmospheric abundances within this region (S.-M. Tsai et al. 2021, 2024; X. Yu et al. 2021; Z. Huang et al. 2024; J. Yang & R. Hu 2024), our calculations are well suited for comparison with JWST data. Second, the relative insolubility of these carbon species in liquid water clouds suggests that their gaseous ratios should undergo minimal change as they move through the water cloud. As a result, our calculated gaseous ratios at the interface with the cloud layer can be directly compared with JWST observations.

3.2. Implications for Habitability

A key question surrounding K2-18 b is whether it can host a habitable environment. Atmospheric observations suggest that the ocean temperature should be at least 710 K to explain the observed carbon ratios, assuming thermochemical equilibrium controls dissolved gas abundances in a supercritical water ocean. Currently, the theoretical upper temperature limit for microbial growth is considered to be $\sim 150^\circ\text{C}$ (423.15 K; D. Schulze-Makuch et al. 2017), indicating that a supercritical water ocean cannot support life as we know it. However, life existing solely within the clouds is a possibility and has been explored for sub-Neptunes by S. Seager & J. J. Petkowski (2021). Although a supercritical water ocean may not permit habitability, studying its chemistry offers a

unique opportunity to understand exotic environments on exoplanets like K2-18 b.

A global supercritical water ocean could foster a hydrothermal environment characterized by hot aqueous fluids. Supercritical fluids have been observed in hydrothermal vent systems on Earth (K. Von Damm et al. 2003; A. Koschinsky et al. 2008); however, we are not implying the presence of individual hydrothermal vents on a rocky seafloor on K2-18 b. Instead, K2-18 b may be a planetary-scale hydrothermal system unlike anything known on Earth. Beyond our planet, similar hydrothermal activity has only been implicated by data from Saturn's moon Enceladus (H.-W. Hsu et al. 2015; J. H. Waite et al. 2017) and hypothesized on Jupiter's moon Europa (M. Běhouňková et al. 2021; M. Melwani Daswani et al. 2021), with no evidence found on an exoplanet to date. While our study does not confirm the existence of hydrothermal processes on K2-18 b, it motivates further investigation into this possibility. The methodology developed here can serve as a first step to investigating hydrothermal worlds.

3.3. Future Work

Our finding is consistent with previous climate models of sub-Neptunes, which suggest that water at the lower boundary would likely exist in a supercritical state rather than

a liquid state (H. Innes et al. 2023; R. T. Pierrehumbert 2023; J. Leconte et al. 2024). Having outlined constraints for a hypothetical supercritical water ocean on K2-18 b, we now turn to the next steps toward an improved understanding of its interior using atmospheric observations.

The most well-constrained abundances from current JWST observations are those of CH₄ and CO₂, which yield a CH₄/CO₂ ratio on the order of unity (N. Madhusudhan et al. 2023b). As these measurements are refined with new data, shifts in this ratio within the error range could occur but may still support the possibility of a supercritical water ocean. Current atmospheric models consistent with the CH₄ and CO₂ observations include a thin-atmosphere liquid water world with biological CH₄ flux, a mini-Neptune lacking a surface influence, and the supercritical hydrothermal water world modeled here. To distinguish between these possibilities, the abundances of CO and NH₃ then become critical factors, as each model predicts different levels of these species (O. Shorttle et al. 2024; N. F. Wogan et al. 2024; J. Yang & R. Hu 2024). Our supercritical water ocean model spans a wide range of CO/CO₂ ratios, but NH₃ was not considered in this study due to the additional complexities involved in modeling its geochemistry. Factors such as ocean pH, total nitrogen inventory, and NH₃ dissolution in water clouds introduce greater uncertainties that make NH₃ more challenging to model compared to the carbon species. Continued study of the phase behavior of H₂-H₂O mixtures under conditions relevant to sub-Neptunes and the development of geochemically practical parameterizations would also be useful next steps.

While current models have brought us closer to understanding K2-18 b's atmospheric structure, more precise constraints on CO and NH₃ abundances will be instrumental for additional testing and refining of our models. Ongoing and future JWST observations (JWST C1 GO 2372, PI: Renyu Hu; JWST C1 GO 2722, PI: Nikku Madhusudhan) will be crucial in providing these constraints, helping to distinguish between the candidate atmosphere-interior structures.

4. Conclusion

Volatile-rich sub-Neptunes have sparked intrigue, with their observed masses and radii hinting at a range of potential interior structures, each carrying distinct implications for the planet's inner workings and the origin of these planets. Recently, transmission spectroscopy of K2-18 b revealed the first detection of CH₄ and CO₂ in the atmosphere of a sub-Neptune exoplanet, along with a nondetection of CO. These data allow us to evaluate the consistency of various structural models against the observed atmospheric composition. In this work, we explored the possibility of K2-18 b being a global hydrothermal world and found the following.

1. A supercritical water ocean with temperatures ranging from approximately 710 K to 1070 K and pressures between 1 and 10 kbar can explain the CH₄/CO₂ ratio observed by JWST and the nondetection of CO.
2. This ocean structure is unlikely to support life as we know it, as the temperature range is far hotter than the upper limit where life has been observed to survive on Earth.
3. The presence of a supercritical water ocean implies that K2-18 b may host a global hydrothermal environment.

Overall, this work corroborates the possibility of K2-18 b being a hydrothermal world and explores how Earth-based geochemical modeling can be a valuable tool for characterizing exoplanet interiors. Future observations that better constrain the abundances of CO and NH₃ will be critical for advancing our understanding of K2-18 b and other temperate sub-Neptunes.

Acknowledgments

X.Y., C.N.L., J.I.M., and J.K.-T. are supported by the NASA Habitable Worlds Program grant 80NSSC24K0075. C.R.G. and N.T. acknowledge support from the Heising-Simons Foundation (grant 2023-4657). X.Y. is supported by the NASA Planetary Science Early Career Award 80NSSC23K1108 and by the Heising-Simons Foundation grant 2023-3936. S.-M.T. is supported by NASA through Exobiology grant No. 80NSSC20K1437 and Interdisciplinary Consortia for Astrobiology Research (ICAR) grant Nos. 80NSSC23K1399, 80NSSC21K0905, and 80NSSC23K1398. X.Z. is supported by the National Science Foundation grant AST2307463 and the NASA Exoplanet Research grant 80NSSC22K0236. A.A. is supported by NASA's Interdisciplinary Consortia for Astrobiology Research (ICAR) grant No. 80NSSC21K0597. H.I. is supported by the European Union (ERC, DIVERSE, 101087755). This work also benefited from the Exoplanet Summer Programs in the Other Worlds Laboratory (OWL) at the University of California, Santa Cruz, a program funded by the Heising-Simons Foundation. We also acknowledge Dr. Ligia Fonseca Coelho for insightful discussions on the temperature range for microbial growth.

Appendix A Observational Data Selection

In this paper, we compare our model predictions against abundances computed using the retrieved one-offset mixing ratio values listed in Table 2 of N. Madhusudhan et al. (2023b). The offset solutions are preferred, as numerous studies have suggested the existence of an offset between the NRS1 and NRS2 detectors of the Near-Infrared Spectrograph instrument used to observe K2-18 b (E. M. May et al. 2023; S. E. Moran et al. 2023). We propagate the uncertainty of the observed ratios using the largest mixing ratio error given for each species. Given the uncertainties in the atmospheric retrieval, it is desirable to adopt the most conservative posture.

Appendix B Conversion between Mass Fraction and Hydrogen Molality

To convert the mass fraction percentages into hydrogen molalities in Section 2.2, we refer to protosolar metallicity values for the H-He mixture consisting of $X_0 = 70.04\%$ H and $Y_0 = 27.80\%$ He (N. Truong et al. 2024). Here, X_0 and Y_0 refer to protosolar mass fractions. If purely H-He is accreted from the protostellar nebula, while excluding all silicate dust and volatile ices, the composition of the gas is 71.58% H and 28.41% He by weight. For a planet with a bulk composition determined by the H-He, H₂O, and rocky core mass fractions $f_{\text{H-He}}$, $f_{\text{H}_2\text{O}}$, and $f_{\text{Rock}} = 1 - f_{\text{H-He}} - f_{\text{H}_2\text{O}}$, respectively, the molality can be computed as follows:

$$m_{\text{H}_2} = \frac{f_{\text{H-He}} X_0}{f_{\text{H}_2\text{O}} X_0 + Y_0 \mu_{\text{H}_2}}, \quad (\text{B1})$$

where μ_{H_2} stands for the molar mass of H₂ in kg · (mol⁻¹).

Appendix C

Detailed Constraints on Hydrogen Molality

Here, we explain how the hydrogen molality (m_{H_2}) range used in our modeling was derived. To determine a reasonable range of m_{H_2} values for our modeling, we first turn toward planet interior structure models to provide a range of possible compositions that match the mass and radius of K2-18 b. This approach provides an independent constraint on the masses of H–He and water, which can be used to estimate the equivalent molality of H_2 for the bulk planet. We assume that this value applies to a supercritical water ocean.

The radius of K2-18 b can be reproduced by end-member cases where the interior is either (i) an Earth-like core with a pure H–He envelope and no water, which corresponds to a hydrogen molality (m_{H_2}) of infinity, or (ii) a nearly 100% water body with no core and negligible amounts of H–He, which leads to $m_{\text{H}_2} \approx 0$ (N. Madhusudhan et al. 2020).

A lower limit on the H_2 molality can be inferred from the ice-to-rock ratio accreted by the planet. If the composition of the interior is inherited from the protoplanetary disk, the latter end-member described above is a highly unlikely scenario. The ice-to-rock ratio in a planet would be controlled by the composition of pebbles/planetesimals in the disk, which is typically made of a mixture of 50% ice and 50% rock (iron and silicates) by mass (J. Drazkowska & Y. Alibert 2017; B. Bitsch & C. Battistini 2020; A. D. Schneider & B. Bitsch 2021; A. Aguichine et al. 2022). Therefore, we place an upper limit on the ice-to-rock content in K2-18 b as 1:1 by mass, similar to the inferred compositions of the icy moons of the solar system (C. Sotin et al. 2007). With this upper limit on the bulk water content, K2-18 b requires a minimal amount (0.02%) of H–He to match its radius (see right panel of Figure 3 from N. Madhusudhan et al. 2020). Such a composition would correspond to a lower limit of $m_{\text{H}_2} = 0.14 \text{ mol} \cdot (\text{kg H}_2\text{O})^{-1}$.

Furthermore, sub-Neptunes should have a limit on how much hydrogen they can accrete during formation. The study of S. Ginzburg et al. (2016) investigated the maximum hydrogen mass fraction retained by the planet according to the core accretion formalism and after an early stage of boil-off. Using their Equation (24), we estimate that the maximum H–He mass fraction accreted by K2-18 b is $\sim 2\%$. However, applying this limit to the interior modeling from N. Madhusudhan et al. (2020) may or may not constitute an additional constraint depending on the assumptions of the interior model, namely, the intrinsic temperature of the planet T_{int} . For $T_{\text{int}} = 25 \text{ K}$, an upper limit of 2% on the H–He will lead to a bulk composition of 2% H–He and 18% H_2O . However, for $T_{\text{int}} = 50 \text{ K}$, only 1.5% of H–He is required to match the bulk density of K2-18 b, meaning that a pure H–He atmosphere cannot be excluded with arguments from interior and formation modeling. Nevertheless, pure H–He envelopes are considered unrealistic, as the hydrogen is expected to react with the FeO component of the silicate mantle to produce H_2O (E. S. Kite et al. 2020; H. E. Schlichting & E. D. Young 2022), and early accretion of planetesimals contributes to the atmosphere's inventory of metals (J. J. Fortney et al. 2013; M. Mol Lous et al. 2024). A bulk composition of 2% H–He and 18% H_2O leads to $m_{\text{H}_2} = 42 \text{ mol} \cdot (\text{kg H}_2\text{O})^{-1}$. In addition, J. Yang & R. Hu (2024) derived a bulk envelope $\text{H}_2\text{O}/\text{H}_2$ ratio through gas-phase chemistry, finding that a scenario in which K2-18 b has $10 \times Z_{\odot}$ with $\text{H}_2\text{O}/\text{H}_2 = 50/50$ is most consistent with observations. This ratio translates to a hydrogen molality of

approximately $56.55 \text{ mol} \cdot (\text{kg H}_2\text{O})^{-1}$. Since this value is close to our upper limit of $42 \text{ mol} \cdot (\text{kg H}_2\text{O})^{-1}$, we choose to adopt $56.55 \text{ mol} \cdot (\text{kg H}_2\text{O})^{-1}$ as an upper limit instead.

Appendix D

Dilute Solution Assumptions in the DEW Model

Our treatment of supercritical water as a dilute solution involves several assumptions that are implicit in our choice of standard states. A standard state is a set of conditions for a species with a fixed chemical composition, serving as a reference state for calculating thermodynamic properties. Often, the standard state is a hypothetical state that may not be physically possible but remains useful in extrapolating thermodynamic properties. We can relate the activities, molalities, and mole fractions through the definitions of standard states from the following equations, adopted from D. A. Sverjensky (2019).

For aqueous species, the relationship between the thermodynamic activity and molality is given by

$$a_j = \frac{\gamma_j m_j}{\gamma_j^0 m_j^0}, \quad (\text{D1})$$

where γ_j and m_j refer to the activity coefficient and molality of species j and γ_j^0 and m_j^0 refer to the standard-state values (G. M. Anderson 2005). We adopt a Henryan standard state (i.e., following Henry's law) known as the “ideal one molal state” for aqueous species. This is a commonly used hypothetical standard state that describes an ideal solution at infinite dilution with $m_j^0 = 1.0$. By definition, real aqueous species cannot physically exist in this state. Under this condition, since $m_j^0 = 1.0$ and $\gamma_j^0 = 1.0$ (see Figure 5 of D. A. Sverjensky 2019), Equation (D1) becomes

$$a_j = \frac{\gamma_j m_j}{(1.0)(1.0)} = \gamma_j m_j. \quad (\text{D2})$$

The ratio of activities for species j and i becomes

$$\frac{a_j}{a_i} = \frac{\gamma_j m_j}{\gamma_i m_i}. \quad (\text{D3})$$

The species of interest in this paper (CH_4 , CO_2 , and CO) are neutral, nonpolar molecules, and while their activity coefficients may depart from unity, the ratio of their activity coefficients tends to cancel out (e.g., T. Barrett et al. 1988). As a result, the ratios of their activities can be approximated as

$$\frac{a_j}{a_i} \approx \frac{m_j}{m_i}. \quad (\text{D4})$$

For water, we adopt a Raoultian standard state (i.e., following Raoult's law) where the fluid phase is pure at some temperature and pressure, and the activity of the ideal solution is equal to its mole fraction. This is the simplest standard state, representing the actual pure phase of the species (G. M. Anderson 2005). Here, the activity of water is related to the mole fraction by the equation

$$a_{\text{H}_2\text{O}} = \lambda_{\text{H}_2\text{O}} X_{\text{H}_2\text{O}}, \quad (\text{D5})$$

where $\lambda_{\text{H}_2\text{O}}$ represents a rational activity coefficient. In the present system, water behaves ideally, and $\lambda_{\text{H}_2\text{O}} \rightarrow 1.0$ as

$X_{\text{H}_2\text{O}} \rightarrow 1.0$; therefore,

$$a_{\text{H}_2\text{O}} \approx X_{\text{H}_2\text{O}}. \quad (\text{D6})$$

The results of Equations (D4) and (D6) are hence substituted into Equations (2) and (4).

Appendix E Generating the P-T Profiles

To generate the P-T profiles, we assume that carbon species equilibrate in a supercritical water ocean at some depth and are then transported upward by turbulent mixing. Eventually, on K2-18 b, these species encounter liquid water droplets higher in the atmosphere. Dissolution into the droplets can change the ratios of species that remain in the gas phase. The temperature profiles at high pressure were assumed to lie on a pure water adiabat. Values for the adiabatic temperature gradient were calculated using the AQUA equation of state for water (J. Haldemann et al. 2020), which provides this quantity tabulated as a function of temperature and pressure. Different profiles were generated by integrating upward from different starting points in the supercritical region of water's phase diagram. The range of profiles reflects the uncertainty in the equilibrium temperature at depth, which would require a more comprehensive coupled radiative transfer and interior model to be determined accurately.

Care was taken in proximity to the liquid–vapor phase boundary, where a discontinuous jump in the adiabatic temperature gradient can produce errors in the data interpolation. Integration was stopped when the temperature was within 10 K of the phase boundary, and the profiles were then linearly interpolated (in logarithmic pressure space) toward the phase boundary. Warmer adiabats that do not intersect this boundary will have hydrogen in much lower concentrations in the upper atmosphere since in this case, there is no cold trapping of water and the hydrogen will be fully miscible with supercritical water

(F. Soubiran & B. Militzer 2015), which is not consistent with the nondetection of water in K2-18 b's atmosphere (N. Madhusudhan et al. 2023b).

Appendix F Parameters for Equilibrium Calculations

The equilibrium constants and Henry's law constants in Equations (2), (4), (6), (8), and (10) are obtained with the DEW model, which uses a series of revised Helgeson–Kirkham–Flowers equations of state for aqueous species (E. L. Shock & H. C. Helgeson 1988, 1990; D. A. Sverjensky et al. 2014) and an equation of state by Z. Zhang & Z. Duan (2005) for water. For convenience, the computed values are then fitted with the logarithmic equation and associated values in Table F1. The equilibrium constants in Equations (2) and (4) are fitted on a linear grid of temperatures between 647.15 K and 1273.15 K at every 1 K following the lower limit, resembling the ocean temperature, at each surface pressure (1000 bars, 5000 bars, 10,000 bars).

The Henry's law constants are initially fitted on a linear grid of temperatures between 444.15 K and 623.15 K at every 1 K. The lower limit represents the lowest temperature at which our P-T profiles cross the saturation boundary, while the upper limit represents DEW's calculation limit at 350°C (623.15 K). To account for our P-T profiles with saturation temperatures reaching up to 647.15 K, we extrapolate the Henry's law constants using the logarithmic equation shown in Table F1 based on the fitting between 444.15 K and 623.15 K. Here, the corresponding pressures are the water-saturated vapor pressures, referred to as “ P_{sat} conditions.” Although this extrapolation introduces some uncertainty, the fitting achieves R^2 values of at least 0.996, demonstrating a close fit to the data. Figure F1 shows the trend of Henry's law constants across the range of temperatures.

Table F1
Summary of Key Chemical Reactions and Parameters to Calculate Equilibrium Constants

Name	Reaction	Pressure (kbar)	R^2	$\log(K) = A + \frac{B}{T} + C \log(T)$		
				A	B	C
Methane–carbon dioxide	$\text{CO}_2(\text{aq}) + 4\text{H}_2(\text{aq}) \rightarrow \text{CH}_4(\text{aq}) + 2\text{H}_2\text{O}(\text{sc})$	1	0.998	81.668	15,682.665	−34.718
		5	0.999	127.989	7364.805	−45.991
		10	0.999	120.328	9699.616	−43.654
Carbon monoxide–carbon dioxide	$\text{CH}_4(\text{aq}) + 4\text{CO}_2(\text{aq}) \rightarrow \text{CO}_2(\text{aq}) + 4\text{CO}(\text{aq}) + 2\text{H}_2\text{O}(\text{sc})$	1	0.999	−36.958	−18,001.432	18.046
		5	0.999	−72.516	−11,110.618	26.572
		10	0.999	−67.254	−12,232.227	24.800
Henry's law for methane	$\text{CH}_4(\text{g}) \rightarrow \text{CH}_4(\text{aq})$	P_{sat} conditions	0.997	−120.131	7106.969	38.224
Henry's law for carbon dioxide	$\text{CO}_2(\text{g}) \rightarrow \text{CO}_2(\text{aq})$	P_{sat} conditions	0.996	−76.414	4775.558	24.016
Henry's law for carbon monoxide	$\text{CO}(\text{g}) \rightarrow \text{CO}(\text{aq})$	P_{sat} conditions	0.998	−121.555	6977.213	38.883

Note. This table presents the parameters for various chemical reactions. The constants A, B, and C are used in the logarithmic equation $\log(K) = A + \frac{B}{T} + C \log(T)$, where T refers to the absolute temperature.

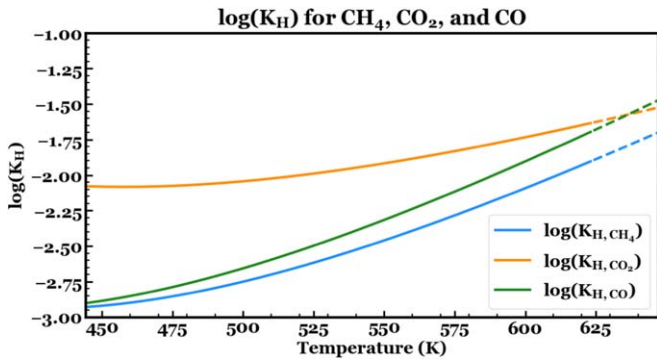


Figure F1. Logarithmically fitted Henry's law constants for CH₄, CO₂, and CO across temperatures between 444.15 K and 623.15 K represented by solid lines, with extrapolated values between 624.15 K and 647.15 K represented by dashed lines. Pressures correspond to water-saturated conditions as shown in Figure 2(a).

Appendix G Caveats

G.1. P-T Profiles of Hydrogen–Water Mixtures

To address the challenges of modeling K2-18 b's interior, we employed a geochemical model to investigate the chemistry of a hypothesized supercritical water ocean on K2-18 b. However, the existing DEW model is limited to water-rich fluids (see the assumptions in Appendix D) and cannot fully account for scenarios with higher hydrogen molalities. It is possible that K2-18 b possesses significantly higher hydrogen molalities than those modeled here. An upper limit on m_{H_2} can be inferred from JWST-derived atmospheric abundances reported by N. Madhusudhan et al. (2023b). The volume mixing ratios of CH₄ and CO₂, each at approximately 1%, provide a lower bound on the bulk volatile content, thus constraining the upper limit on the hydrogen content. Using water as a proxy for all volatiles, this corresponds to an H₂ molality upper limit of 1300 mol · (kg H₂O)⁻¹. Such a high H₂ molality would represent an extremely water-poor fluid, making it incompatible with the present model. To investigate these possible H₂-rich scenarios, conventional gas-phase models (J. Yang & R. Hu 2024) and/or molecular dynamics simulations such as those used in M. Cano Amoros et al. (2024) and A. Gupta et al. (2024) may be more appropriate.

This potential limitation also affects our P-T profiles and the saturation boundary in Figure 2(a) and, consequently, their intersections, where we performed Henry's law calculations. In this work, both the P-T profiles and the saturation boundary were constructed for pure water, or $X_{\text{H}_2\text{O}} = 100\%$. However, K2-18 b's lower atmosphere has $X_{\text{H}_2\text{O}} < 100\%$. In addition, it should be noted that we reference the critical point of pure water rather than that of an H₂–H₂O mixture. To estimate how different H₂–H₂O mixtures might influence the saturation boundary—and, by extension, the crossing temperatures and pressures—we analyzed the saturation boundary corresponding to each mole fraction of water used in this work. We used the REFPROP program (M. L. Huber et al. 2022) to compare the difference in saturation temperatures up to the critical temperature of pure water. The results are summarized in Table G1. We find that these temperature changes are not significant enough to greatly impact our results, given other uncertainties such as the fluid oxidation state (see Appendix D). We note that this calculation does not include nonideal gas

behavior, which becomes more prominent at higher pressures and consequently shifts the crossing temperature; however, changes in crossing temperature also do not matter much in the C–O–H system because solubility corrections applied to exsolved gases are similar (Figure F1). Nevertheless, future work should consider the impact of nonideal phases and incorporate P-T profiles and saturation boundaries that account for the effects of species other than water to achieve a more self-consistent model.

G.2. Carbon Dioxide Mixing Ratio

We assume that gaseous calculations performed for the liquid–vapor interface (cloud bottom) can be directly compared to the JWST observations. However, one notable exception may be CO₂, which can remain in a kinetically controlled balance with quenched CO and H₂O at altitudes above the CO–CH₄–H₂O quench point. In that situation, the CO₂ mixing ratio can often increase with altitude above the quench point, resulting in a CO₂ mole fraction at higher altitudes in excess of expectations based on its deeper equilibrium abundance (R. Hu 2021; X. Yu et al. 2021). Further disequilibrium chemistry gas-phase modeling may be needed to test this scenario.

G.3. Hydrogen–Water Immiscibility?

The pressures and temperatures we explored in this work partially overlap with a region of possible H₂–H₂O immiscibility between 5 kbar and 10 kbar, as shown in Figure 3 of A. Gupta et al. (2024). Instead of a homogeneous layer, H₂–H₂O immiscibility would lead to the formation of two phase-separated layers: an H₂-rich layer on top of an H₂O-rich layer. We performed additional calculations investigating how such phase separation could change our ocean temperature lower limit, which is currently given by the CH₄/CO₂ ratio. In this case, the equilibrium CH₄/CO₂ ratio is determined by the H₂ molality and mole fraction of water in the H₂O-rich layer on the bottom. If H₂ is removed, this layer is expected to contain less dissolved hydrogen than a miscible H₂/H₂O layer, leading to a higher water mole fraction. Thus, we performed sensitivity tests self-consistently varying the mole fraction of water in our model from our highest water mole fraction, $X_{\text{H}_2\text{O}} = 99.6\%$, up to but not including $X_{\text{H}_2\text{O}} = 100.0\%$ for our CH₄/CO₂ ratios at 5 kbar, the lowest pressure for possible immiscibility within our temperature range (A. Gupta et al. 2024). We found that our modeled CH₄/CO₂ ratios still agree with the atmospheric observations, given an ocean temperature lower limit of 710 K, when the mole fraction of water is less than $X_{\text{H}_2\text{O}} = 99.94\%$ ($X_{\text{H}_2} \approx 0.06\%$ or $m_{\text{H}_2} \approx 0.03$ mol · (kg H₂O)⁻¹). However, the lower temperature limit is likely to be immune to the effects of phase splitting, as it is determined by the most water-rich composition (Figure 3(a)). Miscibility can be expected at an H₂ molality of 0.14 mol · (kg H₂O)⁻¹. To decrease our current estimated lower ocean temperature limit below ~710 K, the H₂ molality would need to decrease by a factor of ~5 in a phase-separated H₂O-rich layer to achieve $X_{\text{H}_2\text{O}} = 99.94\%$. Meanwhile, to investigate how our upper limit on temperature may change due to higher water mole fractions in the phase-separated H₂O-rich layer, we performed similar sensitivity tests for our CO/CO₂ ratios at 10 kbar, the highest pressure of interest. Our CO/CO₂ ratios are minimally changed since, as the water mole fraction approaches unity, the proportional increase in CO/CO₂ reaches diminishing returns (Equation (4)).

Table G1
Comparison of H₂-H₂O Compositions and Critical Properties

X _{H₂O}	X _{H₂}	Maximum Difference in T _{sat} (K)	X _{H₂}	Critical Temperature (K)
This work	This work	This work	T. M. Seward & E. U. Franck (1981)	T. M. Seward & E. U. Franck (1981)
99.6%	0.2%	0.26	0.5%	647.45
90.0%	10.0%	8.79	9.0%	647.65
42.4% ^a	43.3% ^a	67.80	40.0%	656.45

Note.

^a Derived from J. Yang & R. Hu (2024) and used in this work. We also note that not all of the H₂O and H₂ mole fractions used here sum to unity because of the addition of helium, while T. M. Seward & E. U. Franck (1981) conducted experiments with H₂-H₂O mixtures excluding helium. The maximum differences from saturated temperatures in this work are computed from the saturation boundary and critical temperature of pure water. Water clouds form at lower temperatures as the atmosphere becomes poorer in water vapor content.






G.4. Supercritical-Liquid Water Adiabats

We find that a portion of our P-T profiles go directly from the supercritical phase to the liquid water phase, as seen by the leftmost adiabat for the 1 kbar pressure in Figure 2(a). This implies a potential interior structure consisting of a hot liquid water layer above a supercritical water layer. However, it is important to note that our P-T profiles do not fully include climate considerations. As mentioned in Section 1, past climate models provide a strong case that surface water on K2-18 b would exist in the supercritical state. H. Innes et al. (2023) considered sub-Neptunes with cloud-free, pure H/He atmospheres receiving solar flux from M stars and found that an atmospheric pressure of 10 bars will lead to a runaway greenhouse effect due to collision-induced absorption. As a result of the runaway greenhouse effect, any liquid water ocean would become supercritical. It has been suggested that surface water can remain liquid in the presence of clouds that provide the necessary albedo (N. Madhusudhan et al. 2023b). Recent studies argue that the high albedo required (>0.5) is both difficult to achieve for K2-18's spectral type and inconsistent with observational data (J. Leconte et al. 2024), although such a high albedo cannot be entirely ruled out (see G. J. Cooke & N. Madhusudhan 2024). These findings support previous interior models suggesting that water-rich sub-Neptunes with a runaway greenhouse effect will develop thick gaseous envelopes with supercritical water (O. Mousis et al. 2020). Therefore, when considering these climate models, we believe it is unlikely for surface water to remain in a liquid state. Our conclusion regarding habitability remains the same for either structure since all adiabats directly entering the liquid phase persist at temperatures above 500 K.

G.5. Species Abundances

Our approach allows us to discern the CH₄/CO₂ and CO/CO₂ ratios that are consistent with observations. However, it is not yet applicable for calculating the mixing ratios of each species, as this requires the detection of carbon-bearing molecules with a higher number of carbon atoms. If future observations detect molecules with more carbon atoms, we can begin to predict the absolute abundances with the DEW model.

ORCID iDs

Cindy N. Luu  <https://orcid.org/0000-0001-5486-1330>
 Xinting Yu (余馨婷)  <https://orcid.org/0000-0002-7479-1437>
 Christopher R. Glein  <https://orcid.org/0000-0002-2161-4672>
 Hamish Innes  <https://orcid.org/0000-0001-5271-0635>
 Artyom Aguichine  <https://orcid.org/0000-0002-8949-5956>

Joshua Krissansen-Totton  <https://orcid.org/0000-0001-6878-4866>

Julianne I. Moses  <https://orcid.org/0000-0002-8837-0035>

Shang-Min Tsai  <https://orcid.org/0000-0002-8163-4608>

Xi Zhang  <https://orcid.org/0000-0002-8706-6963>

Ngoc Truong  <https://orcid.org/0000-0003-2689-3102>

Jonathan J. Fortney  <https://orcid.org/0000-0002-9843-4354>

References

- Aguichine, A., Mousis, O., & Lunine, J. I. 2022, *PSJ*, 3, 141
 Anderson, G. M. 2005, *Thermodynamics of Natural Systems* (2nd ed.; Cambridge: Cambridge Univ. Press),
 Barrett, T., Anderson, G., & Lugowski, J. 1988, *GeCoA*, 52, 807
 Batalha, N. M. 2014, *PNAS*, 111, 12647
 Běhounková, M., Tobie, G., Choblet, G., et al. 2021, *GeoRL*, 48, e2020GL090077
 Benneke, B., Roy, P.-A., Coulombe, L.-P., et al. 2024, arXiv:2403.03325
 Benneke, B., Wong, I., Piaulet, C., et al. 2019, *ApJL*, 887, L14
 Bitsch, B., & Battistini, C. 2020, *A&A*, 633, A10
 Cano Amoros, M., Nettelmann, N., Tosi, N., Baumeister, P., & Rauer, H. 2024, *A&A*, 692, A152
 Cloutier, R., Astudillo-Defru, N., Doyon, R., et al. 2019, *A&A*, 621, A49
 Cooke, G. J., & Madhusudhan, N. 2024, arXiv:2410.07313
 Drazkowska, J., & Alibert, Y. 2017, *A&A*, 608, A92
 Fortney, J. J., Mordasini, C., Nettelmann, N., et al. 2013, *ApJ*, 775, 80
 Fressin, F., Torres, G., Charbonneau, D., et al. 2013, *ApJ*, 766, 81
 Fulton, B. J., & Petigura, E. A., Howard, A. W., et al. 2017, *AJ*, 154, 109
 Ginzburg, S., Schlichting, H. E., & Sari, R. 2016, *ApJ*, 825, 29
 Glein, C. R. 2024, *ApJL*, 964, L19
 Glein, C. R., Zolotov, M. Y., & Shock, E. L. 2008, *Icar*, 197, 157
 Gupta, A., Stixrude, L., & Schlichting, H. E. 2024, arXiv:2407.04685
 Haldemann, J., Alibert, Y., Mordasini, C., & Benz, W. 2020, *A&A*, 643, A105
 Hsu, H.-W., Postberg, F., Sekine, Y., et al. 2015, *Natur*, 519, 207
 Hu, R. 2021, *ApJ*, 921, 27
 Hu, R., Damiano, M., Scheucher, M., et al. 2021, *ApJL*, 921, L8
 Huang, Z., Yu, X., Tsai, S.-M., et al. 2024, *ApJ*, 975, 146
 Huber, M. L., Lemmon, E. W., Bell, I. H., & McLinden, M. O. 2022, *Ind. Eng. Chem. Res.*, 61, 15449
 Innes, H., Tsai, S.-M., & Pierrehumbert, R. T. 2023, *ApJ*, 953, 168
 Kite, E. S., Fegley, J., Bruce, J., Schaefer, L., & Ford, E. B. 2020, *ApJ*, 891, 111
 Koschinsky, A., Garbe-Schönberg, D., Sander, S., et al. 2008, *Geo*, 36, 615
 Leconte, J., Spiga, A., Clément, N., et al. 2024, *A&A*, 686, A131
 Madhusudhan, N., Moses, J. I., Rigby, F., & Barrier, E. 2023a, *FaDi*, 245, 80
 Madhusudhan, N., Nixon, M. C., Welbanks, L., Piette, A. A. A., & Booth, R. A. 2020, *ApJL*, 891, L7
 Madhusudhan, N., Piette, A. A. A., & Constantinou, S. 2021, *ApJ*, 918, 1
 Madhusudhan, N., Sarkar, S., Constantinou, S., et al. 2023b, *ApJL*, 956, L13
 May, E. M., MacDonald, R. J., Bennett, K. A., et al. 2023, *ApJL*, 959, L9
 Melwani Daswani, M., Vance, S. D., Mayne, M. J., & Glein, C. R. 2021, *GeoRL*, 48, e2021GL094143
 Mol Lous, M., Mordasini, C., & Helled, R. 2024, *A&A*, 685, A22
 Moran, S. E., Stevenson, K. B., Sing, D. K., et al. 2023, *ApJL*, 948, L11
 Mousis, O., Deleuil, M., Aguichine, A., et al. 2020, *ApJL*, 896, L22
 Nixon, M. C., & Madhusudhan, N. 2021, *MNRAS*, 505, 3414
 Pierrehumbert, R. T. 2023, *ApJ*, 944, 20
 Rigby, F. E., Pica-Ciamarra, L., Holmberg, M., et al. 2024, *ApJ*, 975, 101

- Rustamkulov, Z., Sing, D. K., Mukherjee, S., et al. 2023, *Natur*, 614, 659
- Scheibe, L., Nettelmann, N., & Redmer, R. 2019, *A&A*, 632, A70
- Schlichting, H. E., & Young, E. D. 2022, *PSJ*, 3, 127
- Schneider, A. D., & Bitsch, B. 2021, *A&A*, 654, A71
- Schulze-Makuch, D., Airo, A., & Schirmack, J. 2017, *FrMic*, 8, 2011
- Seager, S., Petkowski, J. J., Günther, M. N., et al. 2021, *Univ*, 7, 172
- Seward, T. M., & Franck, E. U. 1981, *Ber. Bunsenges. Phys. Chem.*, 85, 2
- Shock, E. L., & Helgeson, H. C. 1988, *GeCoA*, 52, 2009
- Shock, E. L., & Helgeson, H. C. 1990, *GeCoA*, 54, 915
- Shorttle, O., Jordan, S., Nicholls, H., Lichtenberg, T., & Bower, D. J. 2024, *ApJL*, 962, L8
- Sotin, C., Grasset, O., & Mocquet, A. 2007, *Icar*, 191, 337
- Soubiran, F., & Militzer, B. 2015, *HEDP*, 17, 157
- Sverjensky, D. A. 2019, *JGSoc*, 176, 348
- Sverjensky, D. A., Harrison, B., & Azzolini, D. 2014, *GeCoA*, 129, 125
- Truong, N., Glein, C. R., & Lunine, J. I. 2024, *ApJ*, 976, 14
- Tsai, S.-M., Innes, H., Lichtenberg, T., et al. 2021, *ApJL*, 922, L27
- Tsai, S.-M., Innes, H., Wogan, N. F., & Schwieterman, E. W. 2024, *ApJL*, 966, L24
- Von Damm, K., Lilley, M., Shanks, W., et al. 2003, *E&PSL*, 206, 365
- Wagner, W., & Pruß, A. 2002, *JPCRD*, 31, 387
- Waite, J. H., Glein, C. R., Perryman, R. S., et al. 2017, *Sci*, 356, 155
- Wei, J., & Iglesia, E. 2004, *J. Catal.*, 224, 370
- Winn, J. N., & Fabrycky, D. C. 2015, *ARA&A*, 53, 409
- Wogan, N. F., Batalha, N. E., Zahnle, K. J., et al. 2024, *ApJL*, 963, L7
- Yang, J., & Hu, R. 2024, *ApJL*, 971, L48
- Yu, X., Moses, J. I., Fortney, J. J., & Zhang, X. 2021, *ApJL*, 914, 38
- Zhang, Z., & Duan, Z. 2005, *PEPI*, 149, 335